Scientific Research Publishing

Open Journal of Biophysics, 2026, 16(3), 106-132
https://www.scirp.org/journal/ojbiphy
ISSN Online: 2164-5396
ISSN Print: 2164-5388

Automated Malaria Detection and Parasitemia Estimation Using an OpenFlexure Microscope with Integrated Autofocus, Slide Scanning, and Deep Learning

Daniel Maitethia Memeu[1*], Ezekiel Otieno[1], Victoria Muthee[1], Eugene Macharia[1], Patrick Kubai[2], Cynthia N. Mugo Mwenda[3], Dickson Mwenda Kinyua[1,4]

[1]Department of Physical Sciences, Meru University of Science and Technology, Meru, Kenya
[2]Department of Clinical Medicine, Meru University of Science and Technology, Meru, Kenya
[3]Department of Biological Sciences, Meru University of Science and Technology, Meru, Kenya
[4]Department of Pure and Applied Sciences, Kirinyaga University, Kirinyaga, Kenya
Email: *dmaitethia@must.ac.ke

How to cite this paper: Memeu, D.M., Otieno, E., Muthee, V., Macharia, E., Kubai, P., Mwenda, C.N.M. and Kinyua, D.M. (2026) Automated Malaria Detection and Parasitemia Estimation Using an OpenFlexure Microscope with Integrated Autofocus, Slide Scanning, and Deep Learning. *Open Journal of Biophysics*, **16**, 106-132.
https://doi.org/10.4236/ojbiphy.2026.163004

Received: May 27, 2026
Accepted: July 27, 2026
Published: July 30, 2026

Abstract

We present a customized OpenFlexure Microscope (OFM) platform for automated malaria detection and parasitemia estimation. The system integrates a Laplacian variance-based autofocus algorithm optimized for high-magnification (100×/1.25 NA oil immersion) imaging, automated slide scanning, and a YOLOv11n deep-learning model for detection of Plasmodium-infected red blood cells (iRBCs), non-infected red blood cells (RBCs), and white blood cells (WBCs). Approximately 4,000 annotated images acquired from Giemsa-stained *Plasmodium falciparum* thin blood smears were used for model training and evaluation. The proposed autofocus algorithm enabled reliable image acquisition across 100 fields of view, overcoming focus drift observed with the default OpenFlexure autofocus routine. The YOLOv11n model achieved a precision of 70.8%, recall of 91.6%, and F1 score of 79.9% for infected RBC detection. Integrated with automated slide scanning and image analysis, the OFM platform achieved a parasitemia estimation accuracy of approximately 80%, compared with 38% for experienced human microscopists, while reducing analysis time from over 100 minutes to under 40 minutes per slide. The results highlight the challenges associated with reproducible quantitative parasitemia estimation using manual microscopy and demonstrate the advantages of automated image analysis for large-scale cell counting tasks. These findings demonstrate the potential of combining low-cost open-source microscopy with artificial intelligence to provide accurate, reproducible, and scalable malaria parasite detection and parasitemia estimation in resource-

limited and point-of-care settings.

Keywords

Parasitemia, Plasmodium, Edge Devices, Point of Care, YOLO, Autofocusing, Slide Scanning

1. Introduction

Malaria remains a major public health challenge, particularly in sub-Saharan Africa, where it accounts for a significant proportion of morbidity and mortality. Accurate and timely diagnosis is essential for effective treatment and malaria control. Microscopy of Giemsa-stained blood smears remains the gold standard for malaria diagnosis due to its ability to quantify parasitemia and distinguish between Plasmodium species. However, conventional optical microscopy is time-consuming, requires well-trained personnel, and suffers from limited reproducibility, especially in resource-constrained settings.

Recent advances in digital microscopy and artificial intelligence (AI) offer opportunities to overcome these limitations by automating the diagnostic process. Early efforts utilized conventional machine learning algorithms such as Support Vector Machines (SVMs), k-Nearest Neighbors (k-NN), Decision Trees and shallow Artificial Neural Network (ANN) [1]. These methods required manual feature extraction from blood smear images, relying on handcrafted features like color, texture, and shape to differentiate between infected and uninfected cells. While these approaches provided initial automation, their performance was limited by the quality of feature extraction and lacked robustness across diverse datasets.

The advent of deep learning, particularly Convolutional Neural Networks (CNNs), revolutionized image-based malaria diagnosis. CNNs automatically learn hierarchical feature representations from raw pixel data, eliminating the need for manual feature engineering. Architectures like ResNet50 and EfficientNet have demonstrated high accuracy in classifying parasitized and uninfected red blood cells [2]-[8]. A recent study has reported an accuracy of 99.51% in classifying Plasmodium species using a CNN-based model [8].

More recently, transformer-based models, originally developed for natural language processing tasks, have been adapted for image analysis. Vision Transformers (ViTs) and their variants employ self-attention mechanisms to capture global contextual information in images [9] [10]. A notable study proposed a multi-headed attention-based transformer model for malaria parasite detection, achieving high accuracy and offering interpretability through techniques like Grad-CAM [11]. These models have shown promise in capturing complex patterns in blood smear images, potentially outperforming traditional CNNs in certain scenarios.

Despite these advancements, many AI-enabled diagnostic systems are designed for deployment on conventional PCs interfaced with high-end digital microscopes. Such setups are often impractical in rural or low-income settings due to their cost, size, and power requirements. The reliance on powerful computing resources and stable internet connectivity further limits their applicability in resource-constrained environments. To address these challenges, there is a growing interest in deploying AI models on edge devices—compact, low-power hardware capable of performing computations locally. Edge deployment reduces latency, enhances data privacy, and enables real-time diagnostics without the need for continuous internet access.

A few pioneering studies have demonstrated the integration of artificial intelligence (AI) models into edge devices for real-time malaria diagnosis. These efforts represent critical milestones toward the democratization of diagnostic technologies, especially in low-resource settings. One notable example is miLab™, a portable, automated diagnostic platform that integrates a deep learning model on embedded hardware for malaria screening. miLab™ automates slide staining, autofocusing, imaging, and parasite detection. Deployed in field settings in Malawi and Sudan, it achieved a high detection accuracy of 98.86% [12] [13]. While miLab™ is a fully integrated system, it still relies on relatively complex mechanics for slide handling and may not be easily locally fabricated or maintained without specialized components.

Another key contribution is MAIScope—a low-cost, portable microscope enhanced with vision AI, designed to automate malaria diagnostics in rural areas. MAIScope uses a custom CNN model for RBC segmentation and parasite detection, and is operable without internet access. It achieved an average classification accuracy of 89.9%, and was evaluated using a smartphone-attached microscope [14]. However, the system was limited by low image resolution and lacked support for high-magnification imaging (e.g., 100× oil immersion), which is crucial for detecting early-stage (ring form) parasites.

The Mobile Malaria Attention Network (M2ANET) is another lightweight model designed specifically for mobile device deployment. M2ANET combines MobileNetV3 blocks with multi-head self-attention for real-time inference on mobile phones. It outperformed other mobile-compatible networks in accuracy and inference speed [15]. Despite its efficient architecture, M2ANET's validation was primarily done on cropped and preprocessed image patches, without demonstrating full-slide scanning or field-deployable hardware integration. A different study introduced a real-time edge AI system deployed on smartphones to assist in the screening and species differentiation of filarial samples using mobile microscopy [16].

Collectively, these studies mark significant progress in the shift from laboratory-based AI applications to on-device, real-time malaria diagnostics. However, they typically fall short in one or more of the following areas:

i. Limited integration with physical microscopy hardware, especially affordable,

opensource, high-magnification systems like the OpenFlexure Microscope (OFM);

ii. Lack of support for full slide scanning workflows;

iii. Dependence on preprocessed or cropped image datasets, which may not reflect the variability in real-world blood smear slides;

iv. Insufficient field validation across large sample sizes and varied environmental conditions.

The OpenFlexure Microscope (OFM) is an open-source, 3D-printed digital microscope that has gained attention as a low-cost and customizable imaging platform [17]. Its modular design and local manufacturability make it a promising tool for point-of-care (PoC) applications. While the OFM has previously been used for basic imaging tasks [18], its potential for automated diagnostic workflows remains underexplored.

In this study, we present a fully integrated automated malaria detection and parasitemia estimation platform based on the OpenFlexure Microscope (OFM). Our contributions include: (i) the development of a custom Laplacian variance-based autofocusing algorithm optimized for high-magnification (100×/1.25 NA oil immersion) imaging of blood-smear samples; (ii) the integration of a YOLOv11n object detection model for identification and quantification of Plasmodium-infected red blood cells (iRBCs), non-infected red blood cells (RBCs), and white blood cells (WBCs); and (iii) the implementation of a fully automated slide-scanning workflow covering 100 fields of view. The integrated platform was evaluated in terms of object-detection performance, parasitemia estimation accuracy, result reproducibility, and analysis time, and benchmarked against experienced human microscopists. In addition to demonstrating accurate automated parasite detection, the study investigates the challenges associated with reproducible quantitative parasitemia estimation using manual microscopy when large numbers of fields of view must be examined. Our findings demonstrate the potential of combining low-cost open-source microscopy with artificial intelligence to provide scalable malaria detection and parasitemia estimation solutions for resource-limited and point-of-care settings. The image dataset and Python source code used in this work are publicly available through the GitHub repository referenced in [19], while a demonstration video illustrating operation of the prototype system is available through reference [20].

2. Materials and Methods

2.1. Ethical Approval

Ethical approval to conduct the study was sought from Meru University Institutional Research Ethics Review Committee (MIRERC) which is a local ethics review board licensed by the national research regulatory body of Kenya referred to as National Council of Science Technology and Innovation (NACOSTI). Participants in the study were required to give informed consent indicating they have been adequately informed about the goal, methodology and potential benefits and

risks of the study and they willfully and voluntarily decided to participate in the study. The consent agreement also provided for withdrawal from participation at any point of the study. Informed consent by minors participating in the study was made by their guardians.

2.2. Sample Collection and Blood Smear Preparation

Peripheral blood samples were obtained from participants with confirmed *Plasmodium falciparum* infection. *P. falciparum* is the predominant malaria species in the study region and was therefore selected for this study. Each participant donated approximately 2 mL of venous blood, which was collected into EDTA-treated tubes and securely sealed to prevent coagulation. A total of 20 participants contributed blood samples for the study.

From each blood sample, multiple aliquots were used to prepare thin blood smears according to standard malaria microscopy procedures. In total, approximately 400 blood-smear slides were prepared. The smears were air-dried, fixed with methanol, and stained using Giemsa stain. Slides exhibiting adequate staining quality and cellular preservation were selected for image acquisition and analysis. The stained slides were subsequently imaged using the OpenFlexure Microscope (OFM) for the development and evaluation of the automated detection and parasitemia estimation workflow.

2.3. Image Acquisition

Image acquisition was carried out using the OpenFlexure Microscope (OFM), an open-source, low-cost, motorized microscope. Prepared Giemsa-stained thin blood-smear slides were loaded individually onto the microscope stage and secured using the built-in slide clips. The OFM was connected to an external monitor via HDMI to enable real-time visualization, while a keyboard and mouse were connected to facilitate user interaction through the OFM software interface. Once the microscope was powered on, the OFM-Connect application was launched to initiate image acquisition. **Figure 1** shows the experimental setup.

Images were acquired using a Raspberry Pi Camera Module V2 equipped with an 8-megapixel Sony IMX219 image sensor. The camera produced color images with a resolution of 3280 × 2464 pixels and was mounted on a customized OpenFlexure Microscope fitted with a 100×/1.25 NA oil immersion objective lens. Brightfield transmission imaging was performed using the integrated white LED illumination system of the microscope. Camera exposure, gain, illumination intensity, and white balance settings were maintained constant throughout the image acquisition process to ensure consistency across all fields of view and slides.

Prior to imaging, a camera calibration routine including white balance adjustment was performed to ensure accurate representation of stained cellular structures. The microscope stage was also calibrated to establish the relationship between motor steps and physical displacement. This calibration was subsequently used to determine the raster-scanning step size and the autofocus step increments employed during automated image acquisition.

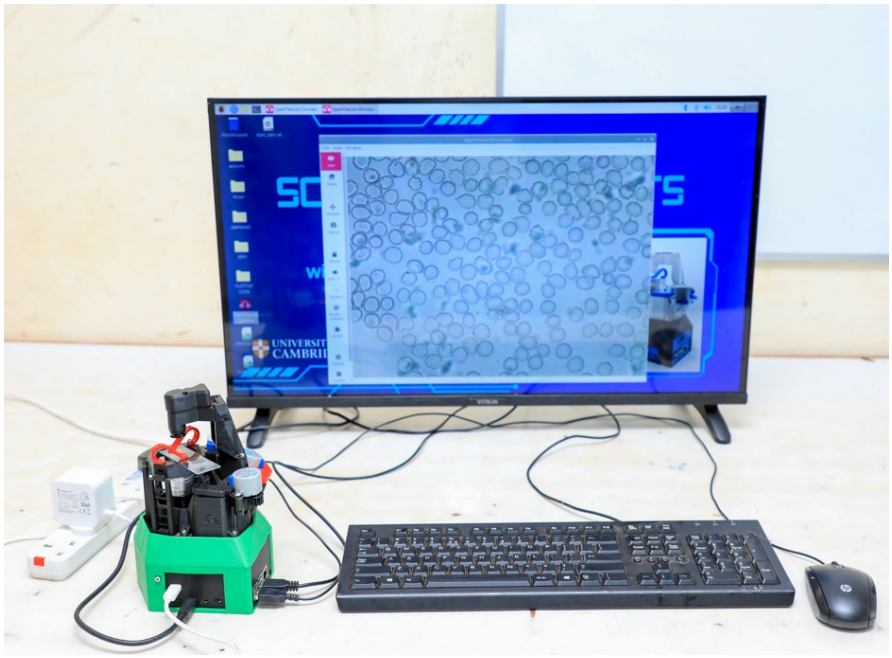

Figure 1. Setup of the customized OpenFlexure Microscope (OFM) for automated malaria diagnosis. A Giemsa-stained blood smear slide is mounted on the sample stage of the OFM. The system is connected to a large LED display via HDMI for real-time image visualization, while a USB keyboard and mouse are used to navigate and control the OFM software interface. The setup enables automated slide scanning, image acquisition, and analysis directly from the microscope platform.

Initial focusing of the first field of view was achieved either manually by adjusting the z-position of the objective lens through the OFM software interface or by using the built-in autofocus function. Once the sample was brought into coarse focus, an automated image acquisition script was executed to capture and save blood-smear images from multiple microscope fields of view (FoVs).

The automated image acquisition workflow consisted of four sequential steps: (i) sample autofocusing, (ii) image capture and saving, (iii) stage translation to a new field of view, and (iv) repetition of the above steps across the entire scan region. A total of 100 fields of view were acquired for each slide.

Slides were scanned using a raster-scanning pattern with a lateral translation step size of 400 motor steps, corresponding to approximately 40 μm of stage displacement between successive fields of view. This step size was selected to provide systematic coverage of the blood smear while minimizing image overlap and redundant sampling.

During preliminary experiments involving automated scanning of Giemsa-stained malaria blood smears using a 100×/1.25 NA oil immersion objective, we observed that the default OpenFlexure autofocus routine frequently produced progressively defocused images after several stage translations. This behavior was attributed to the shallow depth of field associated with high numerical aperture objectives, combined with variations in smear thickness and mechanical backlash during stage movement. Consequently, a custom autofocus algorithm was devel-

oped and integrated into the automated slide-scanning workflow.

The autofocus algorithm employed a coarse-focus search using a step size of 200 motor steps, corresponding to approximately 10 μm of axial displacement, followed by a fine-focus search using a step size of 50 motor steps, corresponding to approximately 2.5 μm of axial displacement. The algorithmic details of the improved autofocus method are described in the following section.

Custom Autofocus Algorithm

The algorithm involves two stages: first, determination of the rough focus direction and position, and second, refinement through fine focus scanning. **Figure 2** presents the algorithmic steps and the description of the steps is provided below.

Rough Focus Determination

When the microscope is translated to a new field of view, the system begins by identifying the approximate focus region through a z-stack acquisition process. The objective lens is first moved downwards, acquiring 10 images at equal intervals with a coarse step size of 200 motor steps (with each step being $\sim 50 \pm 2nm$). The lens is then returned to the initial z-position, after which 10 additional images are acquired in the upward direction using the same step size. This results in a total of 20 z-stack images. For each image in the z-stack, a Laplacian transform is computed, and the **v**ariance of the resulting Laplacian image is calculated. The variance of the Laplacian is evaluated and used as image sharpness metric. Higher variance values indicate sharper images and better focus.

The direction of the sharpness gradient is then analysed as follows: If the variance values have a clear peak between the start and end of the z-stack (*i.e.*, a maximum exists within the 20 images), the corresponding z-position of this peak is identified as the rough focus position. The microscope is moved to this z-position. Else if the variance values show a monotonic increase or decrease across the 20 points (*i.e.*, no peak is detected), the objective is moved one additional step (200 steps) beyond the current endpoint in the direction of increasing variance and additional images are acquired in that direction. At each new z-position: A new image is captured, the Laplacian and its variance are calculated, the variance of the current image is compared to that of the previous position. If the current variance is greater, the objective continues moving in the same direction. Else if the variance decreases, the previous z-position (with the highest variance) is set as the rough focus position.

Fine Focus Determination

To refine the focus, a second z-stack is acquired around the rough focus position: the objective is first moved 200 steps below the rough focus position, and a fine z-stack is then acquired, this time using a smaller step size of 50. The scan continues until the objective is 200 steps above the rough focus position, covering a total of 400 steps. As before, the Laplacian of each image is computed and the variance calculated. The z-position corresponding to the maximum variance within this finer stack is identified as the fine focus position. The microscope is then moved to this position, and the focused image is captured and saved for further processing.

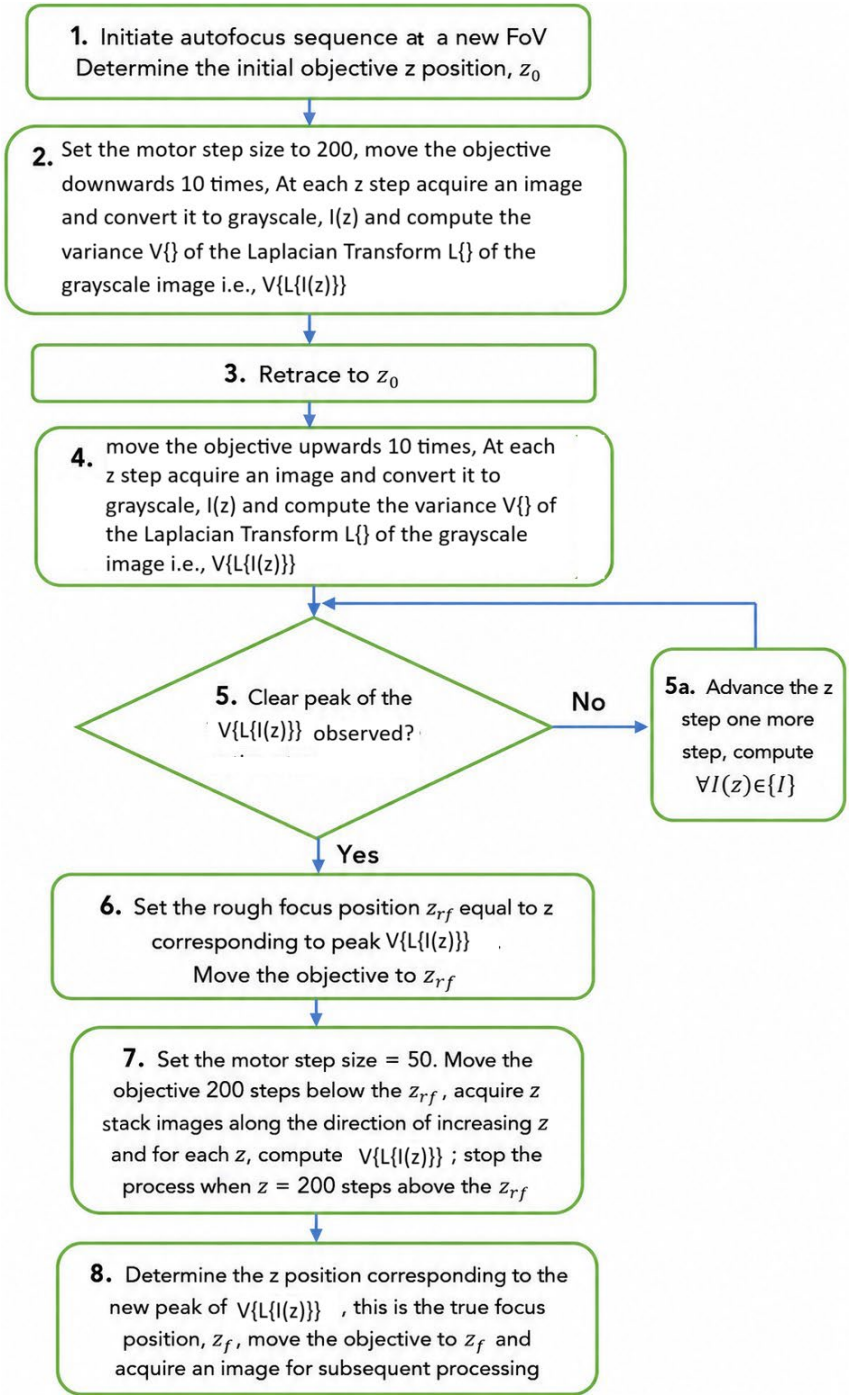

Figure 2. Flowchart illustrating the custom autofocus algorithm implemented on the OpenFlexure Microscope (OFM). The algorithm consists of a two-stage focusing process: rough focus determination through coarse z-stack acquisition and Laplacian variance analysis, followed by fine focus refinement using smaller step-size scanning around the rough focus position.

2.4. Image Annotation

Following the acquisition of blood smear images using the previously described method, image annotation was carried out to generate labelled datasets for ma-

chine learning model training. The annotation process was performed using the Sreeni Image Annotator software [21]. The objective was to classify and label individual cells within each image based on their infection status and cell type. The following procedure was followed:

Class Definition

Three annotation classes were created within the software to guide the labelling process. The classes were; Infected RBC—Red blood cells containing visible Plasmodium parasites, Non-Infected RBC—Red blood cells without any observable signs of infection and WBC—White blood cells present in the blood smear. To facilitate efficient annotation, the acquired images were imported into the annotation software batches and each image was manually reviewed and annotated by marking individual cells with bounding boxes and assigning them to one of the three predefined classes.

Upon completion of the labelling process for each image, annotations were saved in YOLO (You Only Look Once) format, which is suitable for training object detection models. This process was repeated across all batches, resulting in a total of approximately 4000 annotated images. The annotated dataset was periodically reviewed to ensure consistency and accuracy in labelling across images. Any discrepancies identified during the quality checks were corrected to maintain high-quality annotation standards.

2.5. Dataset Preparation

A total of 4000 annotated images were used for training a machine learning model to detect malaria-infected red blood cells. The dataset was split as follows: 70% for training (2800 images), 20% for validation (800 images) and10% for testing (400 images). The dataset was organized using a data.yaml configuration file, which is essential for training YOLO-based models. This file specifies; File paths to images and labels, Class names (e.g., infected RBC, uninfected RBC, WBC) and Dataset splits (train, validation, test)

2.6. Model Training

The YOLOv11n model was selected due to its high speed and efficient performance, making it suitable for real-time object detection on edge devices. Despite its lightweight nature, YOLOv11n achieves a good balance between speed and accuracy.

2.6.1. Model Architecture

YOLOv11n follows the typical YOLO architecture, which consists of three main components:

Backbone

Responsible for extracting features from the input image using convolutional layers. YOLOv11n uses the C3K2 block—an optimized version of Cross Stage Partial (CSP) for faster processing. It also introduces the C2PSA block—which adds

spatial attention to focus on the most relevant regions of an image, enhancing detection accuracy.

Neck

Combines and processes multi-scale features extracted by the backbone. Enhances the model's ability to detect objects of varying sizes. YOLOv11n incorporates improved C3K2 blocks at this stage for better speed and performance.

Head

Generates final predictions, including bounding boxes and class labels for objects (e.g., infected or uninfected RBCs, WBCs).

2.6.2. Training Process

The training process was conducted in a JupyterLab environment on a GPU-enabled workstation equipped with an NVIDIA GPU (driver version 522.06) and 8 GB of memory. The training was executed over 100 epochs, with each epoch taking an average of approximately 247 seconds, resulting in a total training time of around 6.7 hours. The learning process utilized the default YOLO optimizer and learning rate, which is based on the Adam optimizer with an initial learning rate of 0.001.

During training, no data augmentation techniques were applied, as the training framework in use did not support inline augmentation via the command-line interface. The model relied solely on the original distribution of the dataset, which was inherently imbalanced in terms of class frequency. No techniques such as class weighting or oversampling were applied. The model was therefore trained to learn directly from the naturally occurring distribution of infected and uninfected cells.

YOLOv11n optimizes a combination of three loss components during training: classification loss for accurate label prediction, localization loss based on Intersection over Union (IoU) for precise bounding box regression, and objectness loss to evaluate the presence of target objects within bounding boxes. These loss components are built into the YOLO architecture and work together to improve the model's overall detection performance.

Throughout training, the model's performance on the validation set was monitored to avoid overfitting. While no early stopping strategy was explicitly used, the model was capped at 100 epochs, and the best-performing version—based on validation accuracy—was automatically saved in PyTorch format (best.pt). No conversion to other deployment formats (e.g., ONNX or TensorRT) was performed at this stage, as the model was to be deployed within the same PyTorch-compatible environment.

2.7. Model Evaluation Procedure

After training the YOLOv11n model on the annotated blood smear image dataset, the model's performance was evaluated using a systematic validation process. The goal of this evaluation was to assess the model's ability to accurately detect and classify three target cell types: infected red blood cells (RBCs), non-infected RBCs, and white blood cells (WBCs).

A test dataset comprising 20% of the total annotated images was used for performance assessment. This dataset was not exposed to the model during training, ensuring an unbiased evaluation of generalization capability. The evaluation process employed several standard metrics widely used in object detection and classification tasks:

Precision was used to quantify the proportion of true positive predictions out of all positive predictions made by the model. This metric is important for evaluating the model's ability to avoid false positives. Recall was used to measure the proportion of true positive detections out of all actual positive instances in the dataset. It assesses the model's capacity to detect relevant objects comprehensively. Mean Average Precision (mAP) was used to evaluate the model's overall detection accuracy. The mAP score was calculated at different Intersection over Union (IoU) thresholds. mAP@0.5 measures average precision at a fixed IoU threshold of 0.5, while mAP@0.5:0.95 provides a more stringent assessment by averaging precision over multiple IoU thresholds from 0.5 to 0.95 in increments of 0.05.

Loss Metrics were monitored during validation and included bounding box loss (for object localization), segmentation loss (where applicable), and classification loss (for label prediction). These losses provided insights into the model's learning efficiency and convergence behavior. Precision-Confidence and Recall-Confidence Curves were plotted to analyze how model confidence levels affected its performance. These curves helped identify optimal confidence thresholds for reliable predictions. Confusion Matrix analysis was also performed to examine the distribution of true positives, false positives, and false negatives across all three classes. This provided a visual overview of how well the model distinguished between different cell types.

Throughout the evaluation process, model checkpoints and predictions were compared against ground truth annotations prepared during the image annotation phase. The evaluation procedure was conducted using the same YOLO training and inference environment, ensuring consistency in preprocessing and metric computation. This evaluation methodology provided a comprehensive understanding of the model's strengths and limitations and guided further fine-tuning and deployment decisions.

2.8. Model Deployment in the OpenFlexure Microscope (OFM)

After training, the malaria detection model was saved in PyTorch format (model.pt) on the GPU workstation. For deployment, the model was compressed and transferred to a laptop connected to the OpenFlexure Microscope (OFM) system over a local network. The model was then integrated into a custom Python script responsible for controlling the OFM's slide scanning, image acquisition, and analysis.

Upon initiation, the system brings the blood smear slide into focus using an autofocusing algorithm that evaluates image sharpness based on the variance of

the Laplacian. Once the optimal focus is achieved, an image is captured and immediately passed to the malaria detection model for analysis.

The model detects and classifies individual cells as *Plasmodium*-infected red blood cells (iRBCs), non-infected RBCs, or white blood cells (WBCs). It also generates bounding boxes around each detected object, using distinct border colors for different cell classes to facilitate easy verification by a trained microscopist.

The system systematically scans 100 fields of view (FoVs) across the sample, performing autofocusing, image capture, analysis, and result compilation at each location. For each scanned FoV, the number of infected RBCs, non-infected RBCs, and WBCs is recorded, along with the time taken for processing. At the end of the scanning session, the system collates and outputs a diagnostic report summarizing the total and average counts of each cell type across the scanned area.

This deployment enables the OFM to operate as a fully automated malaria diagnostic platform, capable of real-time detection, parasitemia estimation, and generation of verifiable diagnostic outputs from stained blood smear samples.

2.9. Performance Evaluation of the OFM-Based Automated Malaria Diagnostic Platform

To evaluate the performance of the OpenFlexure Microscope (OFM)-based automated malaria detection and parasitemia estimation platform, a comparative study was conducted against conventional manual optical microscopy. The evaluation focused on three key performance indicators: parasitemia estimation accuracy, diagnostic time, and result reproducibility.

Three Giemsa-stained thin blood-smear slides, distinct from those used during model training and validation, were selected for testing. To ensure consistency and fairness, the same diagnostic protocol was applied to both the OFM system and human operators.

2.9.1. Parasitemia Calculation

Parasitemia was calculated as the percentage of infected red blood cells (iRBCs) relative to the total number of red blood cells (RBCs) detected within the analyzed fields of view according to:

$$\text{Parasitemia}\left(\%\right) = \frac{N_{iRBC}}{N_{N\_RBC}} \times 100 \tag{1}$$

where N_{iRBC} is the number of Plasmodium-infected red blood cells and N_{N_RBC} is the total number of red blood cells, calculated as the sum of infected and non-infected RBCs detected within the analyzed fields of view.

2.9.2. Manual Microscopy Evaluation

For the manual microscopy evaluation, three experienced human microscopists were enlisted. Each microscopist examined the three slides using a standard optical microscope equipped with a 100×/1.25 NA oil immersion objective and a 10× eyepiece. The microscopists systematically reviewed 100 fields of

view (FoVs) per slide and recorded the number of infected red blood cells (iRBCs), non-infected red blood cells (RBCs), and white blood cells (WBCs) observed in each field.

The microscopists were required to manually count infected and non-infected red blood cells across all 100 fields of view in order to estimate slide-level parasitemia. This protocol was designed to evaluate the accuracy and reproducibility of quantitative parasite burden assessment rather than simple qualitative malaria detection.

2.9.3. OFM-Based Automated Evaluation

In parallel, the OFM platform performed automated analysis on the same three slides using the integrated autofocusing, slide-scanning, image acquisition, and deep-learning-based cell detection pipeline. For each slide, the system automatically scanned and analyzed 100 fields of view and recorded the number of infected red blood cells, non-infected red blood cells, and white blood cells detected by the YOLOv11n model.

To assess reproducibility, each slide was scanned and analyzed three times under identical imaging conditions using the OFM platform. The consistency of parasitemia estimates across repeated scans was used as a measure of system reproducibility.

2.9.4. Ground-Truth Establishment

To establish reference parasitemia values, three independent image datasets were acquired using the OFM. Each dataset consisted of 300 distinct fields of view per slide, yielding a total of 900 independently acquired fields of view for each test slide.

The image datasets were manually annotated by an experienced microscopist who was not involved in the development, training, or evaluation of the automated detection model. For each image, the number of infected red blood cells, non-infected red blood cells, and white blood cells were recorded. These annotations were subsequently aggregated to determine the ground-truth parasitemia for each slide.

The independently established ground-truth parasitemia values served as the reference standard against which both the OFM platform and the human microscopists were evaluated.

2.9.5. Parasitemia Estimation Accuracy

For each slide, the parasitemia estimated by the OFM platform and by each human microscopist was compared against the corresponding ground-truth parasitemia value.

Parasitemia estimation accuracy was calculated according to:

$$\text{Accuracy}(\%) = \left(1 - \frac{\lceil P_{est} - P_{GT} \rceil}{P_{GT}}\right) * 100 \tag{2}$$

where P_{est} is the estimated parasitemia and P_{GT} is the corresponding ground-

truth parasitemia value. An accuracy value of 100% indicates perfect agreement between the estimated and reference parasitemia values.

2.9.6. Diagnostic Time Evaluation

Diagnostic time was defined as the total time required to analyze a slide and generate a parasitemia estimate. For the OFM platform, this included automated focusing, image acquisition, slide scanning, cell detection, and parasitemia calculation. For manual microscopy, diagnostic time included the time required for slide examination, cell counting, and parasitemia estimation by the microscopists.

2.9.7. Reproducibility Assessment

Reproducibility was assessed by comparing repeated parasitemia measurements obtained from the same slide. For the OFM platform, reproducibility was evaluated using the three repeated automated scans performed under identical conditions. For manual microscopy, reproducibility was assessed by comparing parasitemia estimates obtained from the three independent microscopists.

The variability among repeated measurements was used as an indicator of the consistency and reliability of each approach. Lower variability indicated higher reproducibility and greater robustness of the parasitemia estimation method.

3. Results and Discussion

In this section, we present a comparative analysis of image sharpness and acquisition time for 100 images obtained using the custom-developed autofocusing algorithm versus the built-in autofocus function provided by the OFM client library. We also report the evaluation results of the YOLO-based object detection model used for detecting the specified cellular components in blood smear images. Finally, we compare the diagnostic performance of the customized OFM system against that of expert human-operated microscopy.

3.1. Evaluation of the Custom-Developed Autofocusing Algorithm

The performance of the custom-developed slide scanning and autofocusing algorithm was first evaluated to determine its efficiency and reliability in capturing high-quality, in-focus images across multiple fields of view (FoVs). Autofocusing was a critical component of the system, ensuring sharp imaging necessary for accurate detection of cellular components.

Figure 3 presents sample plots of the variance of the Laplacian computed from z-stack images acquired during the course and fine focusing procedures. Figure 4 compares representative images obtained using the custom autofocus method and the built-in OFM client library autofocus function.

Figure 5 provides a comparison of the variance of the Laplacian—used as a sharpness metric—at various FoVs, along with the total time taken to scan 100 fields using each autofocus strategy.

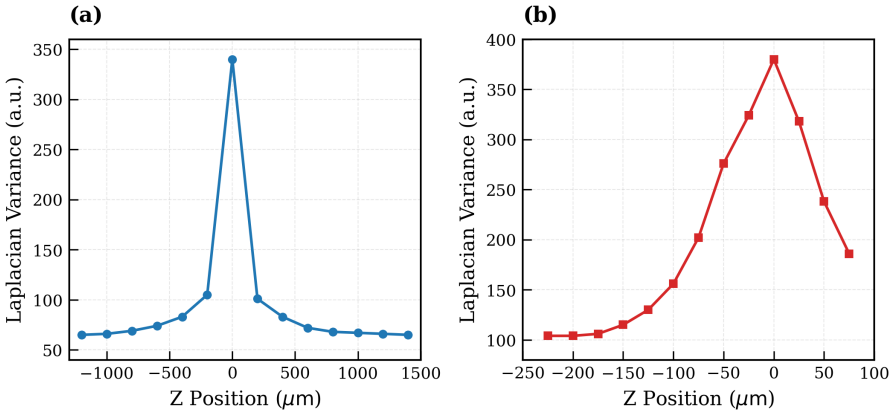

Figure 3. Variance of Laplacian values computed from microscope z-scan images for autofocus determination. (a) Coarse focus scan with a motor step size of 200 units; the z-position corresponding to the peak of the curve indicates the coarse focus position. (b) Fine focus scan with a reduced motor step size of 50 units, performed around the coarse focus position. The best focus is identified by locating the peak variance value between the immediate left and right neighbors of the coarse focus position.

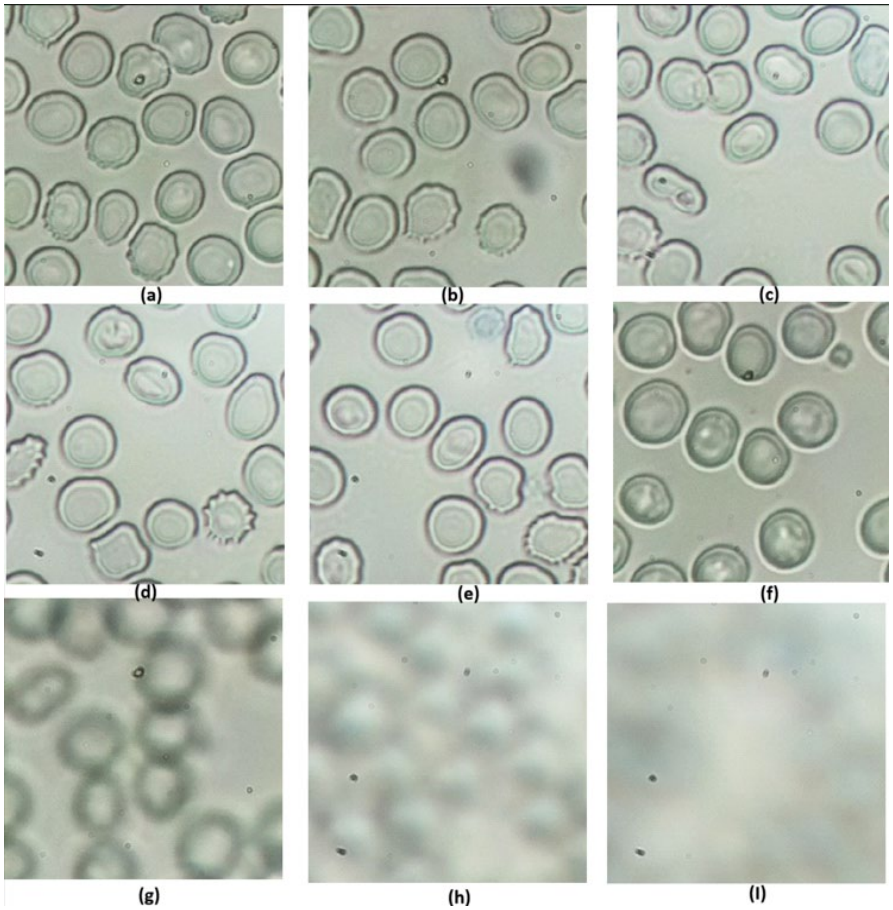

Figure 4. Comparison of best-focus images acquired using the custom-developed autofocus algorithm and the OpenFlexure Microscope (OFM) client library autofocus function. Panels (a)-(e) show images captured at the 1st, 25th, 50th, and 100th fields of view (FOVs) using the custom algorithm, while panels (f)-(i) display images captured at the corresponding FOV positions (1st, 25th, 50th, and 75th) using the OFM client autofocus function.

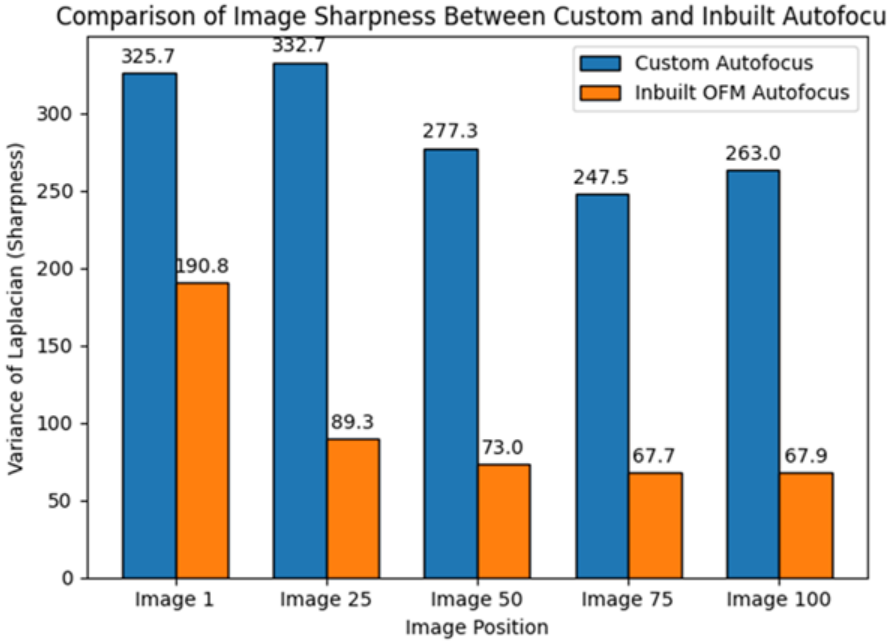

Figure 5. Comparison of image sharpness and scanning time between a custom-developed autofocus algorithm and the OpenFlexure Microscope (OFM) client library autofocus function. Image sharpness was quantified using the variance of the Laplacian of each best-focus image across five representative positions in a 100-field scan. Total scanning time for all 100 images is also reported for each method.

Automatic slide scanning using the OFM's built-in autofocus function often produced out-of-focus images, particularly after small stage translations. As shown in **Figure 3** panels f to I, less than 75% of the 100 acquired images were of insufficient quality for assessing RBC infection status.

In contrast, our custom-developed autofocus algorithm consistently produced sharper images across all 100 fields of view. **Figure 4** panels a to e, shows that all the 100 images acquired from varying microscope FoVs were of sufficient quality to be used to access infection status of the cells. **Figure 5** indicates that the sharpness metric declined more rapidly with the built-in function compared to the custom algorithm for images captured within 100 FoVs.

Image acquisition time was comparable for both methods—approximately 19 minutes for 100 FOVs. However, while most images from the built-in function were unusable, all the images acquired using the custom algorithm found to be usable.

3.2. Evaluation of the Deep Learning Object Detection Model

The YOLOv11n model trained on annotated blood smear images was evaluated using standard performance metrics to assess its detection accuracy, learning convergence, and training stability. A total of 4000 annotated images were used in the training and evaluation process, with the dataset split into 70% for training, 20% for validation, and 10% for testing. The annotations captured three distinct classes: infected red blood cells (RBCs), non-infected RBCs, and white blood cells

(WBCs).

Figure 6 shows the training and validation metrics for your YOLOv11n model across 100 epochs. It's organized into two rows: the top row represents training metrics, and the bottom row represents validation metrics. Each column represents a different metric, giving a comprehensive view of the model's performance.

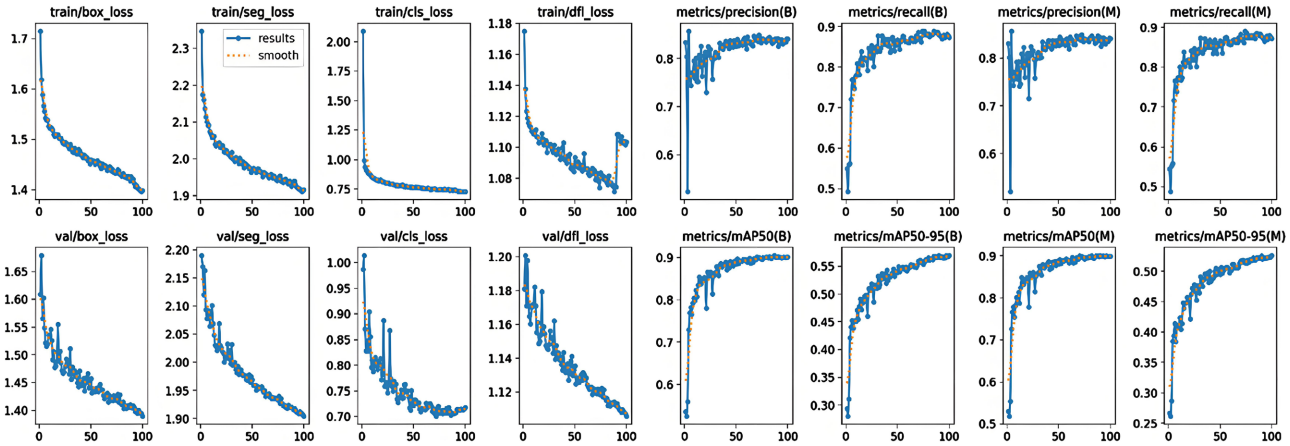

Figure 6. Training and validation performance metrics of the YOLOv11n model over 100 epochs. The top row shows training losses and performance metrics including box loss, segmentation loss, classification loss, distribution focal loss (DFL), precision, and recall. The bottom row presents corresponding validation metrics. Also shown are the mean average precision (mAP) at IoU thresholds 0.5 and 0.5:0.95 for both bounding box detection (B) and mask-based object detection (M). The consistently decreasing loss curves and increasing mAP scores indicate stable learning and improving model performance throughout training.

The following are some general observations regarding the generated training and validation losses. (i) Decreasing Loss: All loss plots (box, seg, cls, dfl) show a decreasing trend, indicating that the model was learning effectively. (ii) Increasing Precision and Recall: Precision and recall for bounding boxes are generally increasing, suggesting the model was improving its detection performance. (iii) Increasing mAP50: The mAP50 is also increasing, reinforcing the positive trends in precision and recall. (iv) Potential for Further Improvement: While the model is performing well, one could consider further optimization techniques (e.g., data augmentation, hyperparameter tuning) to see if you can squeeze out even better performance.

Figure 7 presents the precision-confidence and recall-confidence curves for the three target classes. The model achieved high precision values, particularly at higher confidence thresholds, indicating its ability to make reliable predictions for infected and non-infected RBCs and WBCs.

Table 1 displays the confusion matrix derived from the validation data, highlighting the model's ability to accurately differentiate among the three classes. The highest detection counts lie along the diagonal of the matrix, suggesting correct classification, although a small number of background pixels were occasionally misclassified as non-infected RBCs.

Using values presented in Table 1, the class specific precision, recall, F1 score and overall accuracy was computed and presented in Table 2.

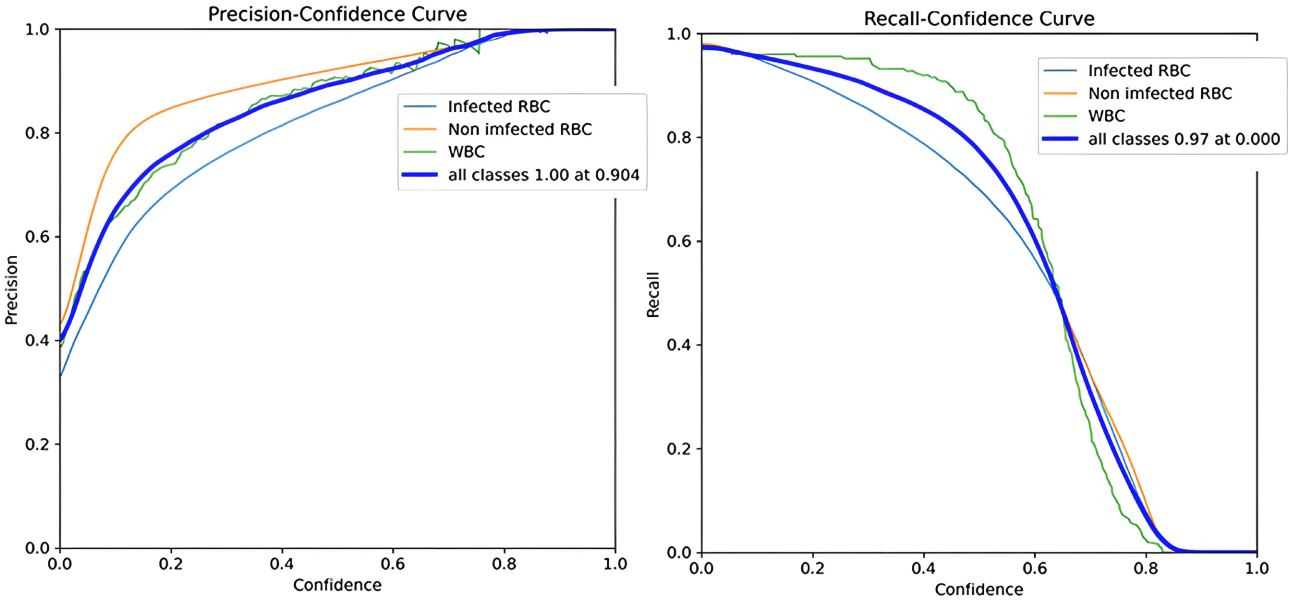

Figure 7. Precision-confidence (left) and recall-confidence (right) curves for the three target classes: infected RBCs, non-infected RBCs, and WBCs. The model demonstrates high precision at elevated confidence thresholds, particularly for non-infected RBCs and WBCs, reflecting its reliability in making accurate predictions.

Table 1. Confusion matrix showing the classification performance of the YOLO-based object detection model for detecting Plasmodium-infected red blood cells (RBCs), non-infected RBCs, white blood cells (WBCs), and background. The diagonal elements represent correctly classified instances for each class, while off-diagonal values indicate misclassifications.

	True: Infected RBC	Non-infected RBC	WBC	Background
Pred: Infected RBC	65,868	10,504	0	16,673
Pred: Non-infected RBC	6,014	199,892	1	28,313
Pred: WBC	1	2	239	60

Table 2. Class-wise precision, recall, and F1 score for the YOLO-based object detection model in identifying Plasmodium-infected red blood cells (RBCs), non-infected RBCs, and white blood cells (WBCs). The model achieved the highest recall for WBCs (99.6%) and the highest F1 score for non-infected RBCs (89.9%), indicating robust performance in differentiating cell types. The overall model accuracy across all classes was 81.2%.

Class	Precision	Recall	F1 Score
Infected RBC	0.707916	0.916322	0.798749
Non-infected RBC	0.853437	0.950066	0.899163
WBC	0.791391	0.995833	0.881919
Overall accuracy			0.812045

The YOLOv11n model demonstrated strong performance across all three cell classes. For infected RBC detection, the model achieved a precision of 70.8%, recall of 91.6%, and F1 score of 79.9%. The high recall indicates that the majority of infected cells were successfully detected, minimizing the risk of missed infections. For non-infected RBC detection, the model achieved a precision of 85.3%, recall

of 95.0%, and F1 score of 89.9%. White blood cell detection achieved a precision of 79.1%, recall of 99.6%, and F1 score of 88.2%, representing the highest recall among all evaluated classes. Overall, these results demonstrate the ability of the model to reliably distinguish infected RBCs, non-infected RBCs, and WBCs in Giemsa-stained thin blood-smear images.

These metrics are significant in the context of a disease diagnostic model because:

- Precision reflects how many of the cells identified as infected were actually infected, which is critical for reducing false positives that may lead to unnecessary treatment.
- Recall (or sensitivity) indicates how many of the truly infected cells were successfully detected by the model. A recall of 70.8% suggests that while the model is effective, there is still room for improvement in capturing all true cases, which is vital for early and accurate malaria diagnosis.
- F1 Score, the harmonic mean of precision and recall, provides a balanced measure of the model's diagnostic performance.

Compared to manual microscopy, which has a reported sensitivity of 75% - 90% when performed by expert microscopists, the model's sensitivity is within an acceptable range, especially considering its automation potential. In contrast, Rapid Diagnostic Tests (RDTs) typically show lower sensitivity—often between 60% - 75%—and may fail to detect low parasite densities. Therefore, this automated model demonstrates a promising balance of accuracy and scalability, with the potential to augment or even outperform traditional diagnostic methods in resource-limited settings, especially when deployed on portable systems like the OpenFlexure Microscope.

The image in **Figure 8** illustrates one of the detection output from the automated malaria diagnostic system, in which a YOLOv11n object detection model has classified individual red blood cells (RBCs) based on infection status. Red bounding boxes highlight RBCs identified as *Plasmodium*-infected, while yellow bounding boxes indicate non-infected RBCs. Infected cells exhibit characteristic morphological features such as the presence of dark-staining ring forms, cytoplasmic inclusions, or altered cell shape and texture—hallmarks of intraerythrocytic *Plasmodium* parasites. In contrast, non-infected RBCs typically display a uniform round shape with a central pale zone (biconcave appearance) and lack any internal inclusions or distortions. The detection pattern demonstrates the model's ability to differentiate subtle visual cues across a densely populated field, thereby enabling accurate parasitemia quantification in a manner consistent with expert microscopy assessment. The different color of bounding boxes aid in counterchecking the correctness of the results provided by automated system. The system is programmed to count the total infected RBCs, non-infected RBCs and white blood cells detected in 100 FoV automatically scanned. Parasitemia; which is the ratio of infected to non-infected RBCs is also then computed and displayed on the screen.

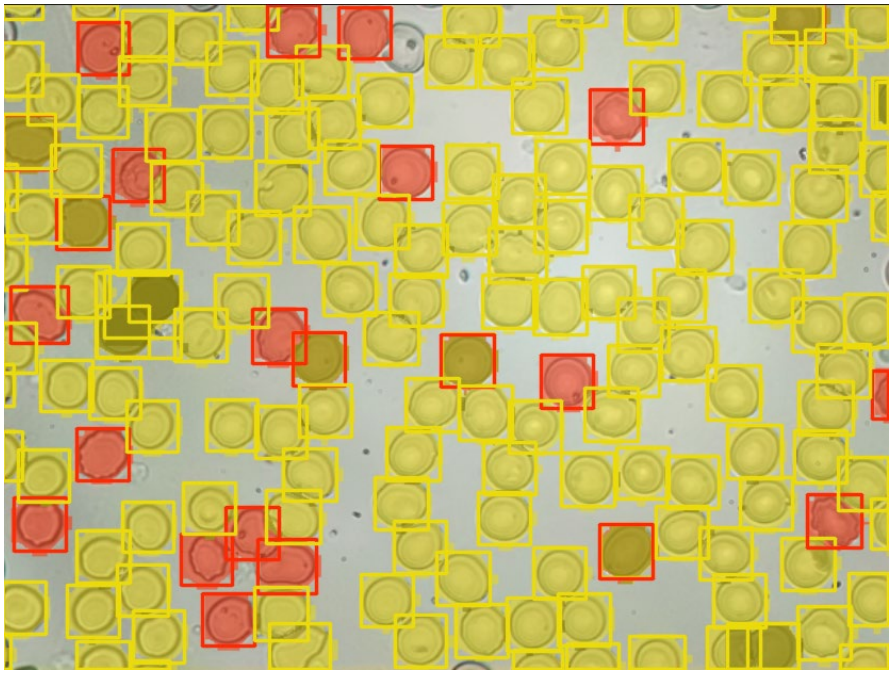

Figure 8. Representative output image from the automated malaria diagnostic system showing the results of object detection using the YOLOv11n model. Red bounding boxes indicate red blood cells (RBCs) identified as Plasmodium-infected, while yellow bounding boxes represent non-infected RBCs. The system accurately detects and classifies individual cells across the field of view, supporting reliable parasitemia estimation.

3.3. Comparative Diagnostic Study

The fully integrated OFM-based malaria detection and parasitemia estimation platform was evaluated alongside three experienced human microscopists. The evaluation focused on parasitemia estimation accuracy relative to independently established ground-truth values, diagnostic time per slide, and reproducibility across repeated measurements.

Figure 9 compares the average parasitemia estimation accuracy achieved by the OFM-based system and the human microscopists. The OFM platform achieved an average parasitemia estimation accuracy of 80.3%, whereas the human microscopists achieved an average accuracy of 38.0%. In addition, the OFM system exhibited lower variability across repeated analyses, as evidenced by the smaller standard deviation shown in **Figure 9**. These findings indicate that the automated platform produced more consistent and reproducible parasitemia estimates than manual microscopy.

It is important to note that the reported accuracy values refer to quantitative parasitemia estimation (Equation (1)) rather than binary malaria diagnosis. In this study, microscopists were required to examine 100 fields of view per slide and estimate parasitemia by counting infected and non-infected red blood cells. Such quantitative assessments are susceptible to sampling variability, counting errors, and observer fatigue, particularly when large numbers of fields of view must be examined. The lower agreement observed among human microscopists therefore reflects the challenges associated with reproducible parasite burden quantification

rather than an inability to recognize malaria infection.

The OFM system also demonstrated substantial improvements in workflow efficiency. The average time required for automated analysis of a slide was approximately 40 minutes, compared with approximately 1 hour and 40 minutes for manual microscopy. The reduction in analysis time was achieved through the integration of automated autofocus, raster scanning, image acquisition, and deep-learning-based cell detection within a single workflow.

To further evaluate diagnostic performance, an independent validation study involving 100 clinical blood-smear slides was conducted. The dataset comprised 46 malaria-positive slides and 54 malaria-negative slides. Table 3 summarizes the comparative diagnostic performance of the OFM platform and human microscopists.

The OFM platform correctly identified all 46 malaria-positive slides and all 54 malaria-negative slides, corresponding to a sensitivity of 100%, specificity of 100%, and overall diagnostic accuracy of 100% within the evaluated cohort. In contrast, the human microscopists correctly identified 8 of the 46 malaria-positive slides and all 54 malaria-negative slides, yielding a sensitivity of 17.4%, specificity of 100%, and overall diagnostic accuracy of 62.0%.

These results indicate that while the human microscopists were highly effective at recognizing malaria-negative slides, a substantial proportion of malaria-positive slides were incorrectly classified as negative. The OFM platform successfully detected all positive and negative slides in the validation cohort, demonstrating its potential to reduce false-negative diagnoses and improve the reliability of malaria screening, particularly in low-parasitemia cases.

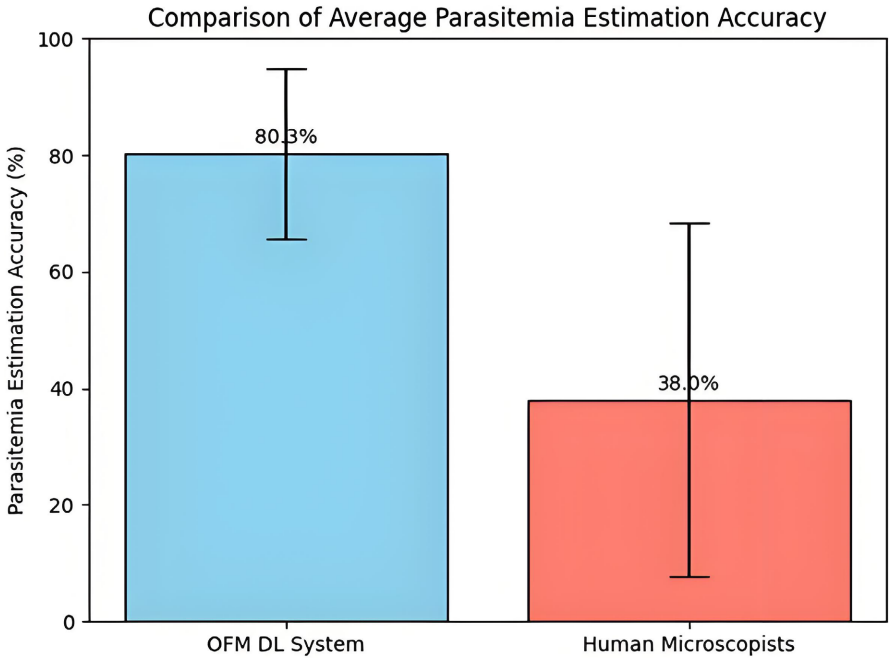

Figure 9. Comparison of average parasitemia estimation accuracy between the OFM-based deep learning system and human microscopists. Error bars represent standard deviations calculated from three independent evaluations per system.

Table 3. Diagnostic performance of the OFM platform and human microscopists on an independent validation cohort of 100 blood-smear slides.

1	OFM Positive	OFM Negative	Human Positive	Human Negative
Malaria Positive (n = 46)	46	0	8	38
Malaria Negative (n = 54)	0	54	0	54

These results demonstrate that the ML enabled OFM platform not only provides more accurate and reproducible parasitemia estimation but also substantially improves the detection of low-parasitemia infections that may be missed during routine manual examination. The findings highlight the potential of combining automated microscopy and deep learning to support malaria screening and quantitative parasite burden assessment in resource-limited settings.

4. Discussion

Our custom-developed autofocus algorithm, implemented on the OpenFlexure Microscope (OFM), combines coarse and fine z-stack scanning with Laplacian variance-based sharpness estimation to achieve reliable focusing during automated slide scanning. Unlike the default OFM autofocus routine, which frequently produced progressively defocused images during extended scans using a 100×/1.25 NA oil immersion objective, the proposed approach maintained image quality across 100 fields of view. The improved performance is attributable to the two-stage focusing strategy, which first identifies the approximate focal region and subsequently refines the focus position using smaller axial step sizes. This capability is particularly important for malaria microscopy, where the shallow depth of field associated with high numerical aperture objectives makes image quality highly sensitive to small variations in slide thickness and mechanical stage positioning.

Compared with previously reported OFM autofocus approaches, our method offers a practical balance between robustness, computational simplicity, and ease of deployment. Unlike hardware-based autofocus systems that require additional optical components and calibration procedures, the proposed algorithm can be implemented entirely through software using existing OFM hardware. This makes it particularly suitable for low-resource settings where affordability, maintainability, and local manufacturability are important considerations.

The YOLOv11n object detection model demonstrated strong performance in identifying infected red blood cells (iRBCs), non-infected red blood cells (RBCs), and white blood cells (WBCs). For infected RBC detection, the model achieved a precision of 70.8%, recall of 91.6%, and F1 score of 79.9%. The high recall indicates that the model successfully detected the vast majority of infected cells, minimizing the risk of missed infections. This characteristic is particularly important in malaria screening applications, where failure to identify infected cells may lead to underestimation of parasite burden. The lower precision indicates the presence of some false-positive detections, suggesting opportunities for further improve-

ment through expansion of the training dataset and incorporation of additional examples exhibiting staining artefacts and morphological variability.

It is important to note that the primary objective of the YOLOv11n model was object-level detection and classification of cellular components rather than patient-level diagnosis. The model was trained to recognize cellular morphology associated with infected RBCs, non-infected RBCs, and WBCs. Consequently, the risk of participant-specific information leakage is expected to be lower than in studies involving direct patient-level disease classification. Nevertheless, future studies would benefit from participant-level dataset partitioning to provide a more rigorous assessment of model generalization performance.

The fully integrated OFM-based platform demonstrated promising performance for automated malaria analysis. By combining autofocus, automated slide scanning, image acquisition, object detection, and parasitemia estimation within a single workflow, the system eliminates many of the manual steps traditionally required for microscopy-based malaria assessment. Unlike many previous AI-based malaria studies that relied on pre-acquired image datasets, the present work evaluated the complete end-to-end diagnostic workflow from slide loading to result generation.

A key finding of this study was the substantial difference observed between automated and manual parasitemia estimation. The OFM system achieved an average parasitemia estimation accuracy of approximately 80%, whereas experienced human microscopists achieved an average accuracy of 38% relative to independently established ground-truth parasitemia values. This observation should not be interpreted as evidence that experienced microscopists are poor at malaria diagnosis. Rather, it highlights the challenges associated with quantitative parasitemia estimation when large numbers of fields of view must be examined. In our study, microscopists were required to evaluate 100 fields of view per slide and estimate parasitemia based on counts of infected and non-infected red blood cells. Such quantitative counting tasks are inherently susceptible to sampling variability, counting errors, and observer fatigue. The results therefore suggest that automated image analysis may provide substantial advantages in reproducibility and consistency when quantitative parasite burden assessment is required.

The findings are further supported by the low variability observed across repeated OFM analyses compared with the larger variability observed among human readers. This improved reproducibility is particularly important because parasitemia estimation is widely used to assess disease severity, monitor treatment response, and support clinical decision-making. Automated approaches that reduce observer-dependent variability may therefore improve the reliability of parasite burden assessment in both clinical and research settings.

The computational efficiency of YOLOv11n also contributed to the practical utility of the system. In the present study, all model inference and diagnostic performance evaluations were performed on a laptop computer connected to the OpenFlexure Microscope, while the embedded Raspberry Pi was used solely for

microscope control, image acquisition, and stage movement. Although Raspberry Pi-based inference was not evaluated in this work, the lightweight architecture of YOLOv11n suggests that future deployment on embedded edge-computing platforms may be feasible, potentially enabling fully self-contained diagnostic systems for point-of-care use.

Several limitations should be acknowledged. First, all blood samples included in this study originated from patients with confirmed Plasmodium falciparum infection, and therefore the performance of the system on other Plasmodium species remains unknown. Second, dataset partitioning was performed at the image level rather than participant level. Although this is less concerning for object-level cell detection than for patient-level classification tasks, future studies should evaluate participant-level splits to provide a more rigorous assessment of model generalization. Third, the study focused primarily on parasite detection and parasitemia estimation from Giemsa-stained thin blood smears; additional validation across larger and more geographically diverse cohorts will be required before widespread clinical deployment.

Despite these limitations, the results demonstrate that a customized OpenFlexure Microscope integrated with automated focusing, slide scanning, and deep-learning-based image analysis can provide accurate, reproducible, and efficient malaria parasite detection and parasitemia estimation. The combination of low-cost open-source hardware and artificial intelligence offers a promising pathway toward scalable malaria diagnostics in resource-limited settings.

5. Conclusions

This study developed and evaluated an automated malaria blood-smear analysis platform based on a customized OpenFlexure Microscope (OFM). The system integrates a custom Laplacian variance-based autofocus algorithm, automated slide scanning, and a YOLOv11n object detection model for the identification of infected red blood cells (iRBCs), non-infected red blood cells (RBCs), and white blood cells (WBCs). The proposed autofocus strategy maintained reliable image quality across 100 fields of view and enabled robust high-magnification imaging using a 100×/1.25 NA oil immersion objective.

The integrated platform achieved a parasitemia estimation accuracy of approximately 80%, compared with 38% for experienced human microscopists, while reducing analysis time from over 1 hour and 40 minutes to under 40 minutes per slide. These findings highlight not only the effectiveness of the automated approach but also the challenges associated with reproducible quantitative parasitemia estimation using manual microscopy when large numbers of fields of view must be examined. The lower variability observed across repeated OFM analyses further demonstrates the potential of automated image analysis to improve consistency and reproducibility in parasite burden assessment.

Overall, the results demonstrate that low-cost open-source microscopy combined with deep learning can provide an effective platform for automated malaria

parasite detection and parasitemia estimation. Future work will focus on validating the system across larger and more geographically diverse cohorts, evaluating performance on additional Plasmodium species, and exploring deployment of the detection model on embedded edge-computing hardware to enable fully self-contained point-of-care diagnostic systems.

Funding

Academy of Medical Sciences Networking Grant (NGR1\1211), funded by the UK Department for Science, Innovation and Technology (DSIT) through the International Science Partnerships Fund (ISPF).

Acknowledgment

The authors gratefully acknowledge the Academy of Medical Sciences for providing partial funding to support this research. We also extend our sincere appreciation to Professor Pietro Cicuta of University of Cambridge for his invaluable role in supporting capacity building, particularly in the acquisition of skills related to the fabrication and customization of the OpenFlexure Microscope.

Disclosures

The authors declare that there is no conflict of interest regarding the publication of this work.

Data Availability

Data and source code underlying the results presented in this paper are available in a public GitHub repository: https://github.com/EzekielOtieno/Malaria (Ref. [19]).

Conflicts of Interest

The authors declare no conflicts of interest regarding the publication of this paper.

References

[1] Poostchi, M., Silamut, K., Maude, R.J., Jaeger, S. and Thoma, G. (2018) Image Analysis and Machine Learning for Detecting Malaria. *Translational Research*, **194**, 36-55. https://doi.org/10.1016/j.trsl.2017.12.004

[2] Madhu, G., Mohamed, A.W., Kautish, S., Shah, M.A. and Ali, I. (2023) Intelligent Diagnostic Model for Malaria Parasite Detection and Classification Using Imperative Inception-Based Capsule Neural Networks. *Scientific Reports*, **13**, Article No. 13377. https://doi.org/10.1038/s41598-023-40317-z

[3] Kumar, S., Arif, T., Alotaibi, A.S., Malik, M.B. and Manhas, J. (2022) Advances towards Automatic Detection and Classification of Parasites Microscopic Images Using Deep Convolutional Neural Network: Methods, Models and Research Directions. *Archives of Computational Methods in Engineering*, **30**, 2013-2039. https://doi.org/10.1007/s11831-022-09858-w

[4] Elayaraja, S., Yeruva, S., Stejskal, V. and Nandipati, S. (2024) Multi-Class Microscopic

Image Analysis of Protozoan Parasites Using Convolutional Neural Network. *Journal of Universal Computer Science*, **30**, 420-432. https://doi.org/10.3897/jucs.112639

[5] Rahman, A., Zunair, H., Reme, T.R., Rahman, M.S. and Mahdy, M.R.C. (2021) A Comparative Analysis of Deep Learning Architectures on High Variation Malaria Parasite Classification Dataset. *Tissue and Cell*, **69**, Article 101473. https://doi.org/10.1016/j.tice.2020.101473

[6] Khan, S.H., Shah, N.S., Nuzhat, R., Majid, A., Alquhayz, H. and Khan, A. (2022) Malaria Parasite Classification Framework Using a Novel Channel Squeezed and Boosted CNN. *Microscopy*, **71**, 271-282. https://doi.org/10.1093/jmicro/dfac027

[7] Kudisthalert, W., Pasupa, K. and Tongsima, S. (2020) Counting and Classification of Malarial Parasite from Giemsa-Stained Thin Film Images. *IEEE Access*, **8**, 78663-78682. https://doi.org/10.1109/access.2020.2990497

[8] Ramos-Briceño, D.A., Flammia-D'Aleo, A., Fernández-López, G., Carrión-Nessi, F.S. and Forero-Peña, D.A. (2025) Deep Learning-Based Malaria Parasite Detection: Convolutional Neural Networks Model for Accurate Species Identification of *Plasmodium falciparum* and Plasmodium Vivax. *Scientific Reports*, **15**, Article No. 3746. https://doi.org/10.1038/s41598-025-87979-5

[9] Tan, D. and Liang, X. (2023) Multiclass Malaria Parasite Recognition Based on Transformer Models and a Generative Adversarial Network. *Scientific Reports*, **13**, Article No. 17136. https://doi.org/10.1038/s41598-023-44297-y

[10] Islam, M.R., Nahiduzzaman, M., Goni, M.O.F., Sayeed, A., Anower, M.S., Ahsan, M., *et al.* (2022) Explainable Transformer-Based Deep Learning Model for the Detection of Malaria Parasites from Blood Cell Images. *Sensors*, **22**, Article 4358. https://doi.org/10.3390/s22124358

[11] Sengar, N., Burget, R. and Dutta, M.K. (2022) A Vision Transformer Based Approach for Analysis of Plasmodium Vivax Life Cycle for Malaria Prediction Using Thin Blood Smear Microscopic Images. *Computer Methods and Programs in Biomedicine*, **224**, Article 106996. https://doi.org/10.1016/j.cmpb.2022.106996

[12] Bae, C.Y., Shin, Y.M., Kim, M., Song, Y., Lee, H.J., Kim, K.H., *et al.* (2024) Embedded-Deep-Learning-Based Sample-to-Answer Device for On-Site Malaria Diagnosis. *Frontiers in Bioengineering and Biotechnology*, **12**, Article 1392269. https://doi.org/10.3389/fbioe.2024.1392269

[13] Hamid, M.M.A., Mohamed, A.O., Mohammed, F.O., Elaagip, A., Mustafa, S.A., Elfaki, T., *et al.* (2024) Diagnostic Accuracy of an Automated Microscope Solution (miLab™) in Detecting Malaria Parasites in Symptomatic Patients at Point-of-Care in Sudan: A Case-Control Study. *Malaria Journal*, **23**, Article No. 200. https://doi.org/10.1186/s12936-024-05029-3

[14] Sangameswaran, R. (2022) MAIScope: A Low-Cost Portable Microscope with Built-In Vision AI to Automate Microscopic Diagnosis of Diseases in Remote Rural Settings.

[15] Ali, S.A., Abdulqadir, P.S., Abdullah, S.A., *et al.* (2024) M2ANET: Mobile Malaria Attention Network for Efficient Classification of *Plasmodium* Parasites in Blood Cells.

[16] Lin, L., Dacal, E., Díez, N., Carmona, C., Martin Ramirez, A., Barón Argos, L., *et al.* (2024) Edge Artificial Intelligence (AI) for Real-Time Automatic Quantification of Filariasis in Mobile Microscopy. *PLOS Neglected Tropical Diseases*, **18**, e0012117. https://doi.org/10.1371/journal.pntd.0012117

[17] Collins, J.T., Knapper, J., Stirling, J., Mduda, J., Mkindi, C., Mayagaya, V., *et al.* (2020)

Robotic Microscopy for Everyone: The Open Flexure Microscope. *Biomedical Optics Express*, **11**, 2447-2460. https://doi.org/10.1364/boe.385729

[18] Rosen, D.G., de Mello, E.S., Dhingra, S., Dawsey, S.M., Knapper, J., Bowman, R., *et al.* (2024) Utility of a Low-Cost 3-D Printed Microscope for Evaluating Esophageal Biopsies. *Annals of 3D Printed Medicine*, **13**, Article 100145. https://doi.org/10.1016/j.stlm.2024.100145

[19] Github Repository. https://github.com/EzekielOtieno/OFM

[20] Video Demo. https://youtu.be/V6t1UBeD_IE?si=WcMGGRzAI7RSNoDw

[21] Sreeni Image Annotation Tool. https://github.com/bnsreenu/digitalsreeni-image-annotator